IOP Publishing Nanotechnology
Nanotechnology 32 (2021) 215701 (6pp) https://doi.org/10.1088/1361-6528/abe438

High-performance ambipolar MoS_2 transistor enabled by indium edge contacts

Hai Yen Le Thi[1], Muhammad Atif Khan[2], A Venkatesan[3], Kenji Watanabe[4], Takashi Taniguchi[5] and Gil-Ho Kim[1,3]

[1] Sungkyunkwan Advanced Institute of Nanotechnology (SAINT), Sungkyunkwan University (SKKU), Suwon 16419, Republic of Korea
[2] Department of Electrical and Computer Engineering, Air University, Sector E-9, Islamabad, Pakistan
[3] School of Electronic and Electrical Engineering, Sungkyunkwan University (SKKU), Suwon 16419, Republic of Korea
[4] Research Center for Functional Materials, National Institute for Materials Science, 1-1 Namiki, Tsukuba 305-0044, Japan
[5] International Center for Material Nanoarchitectonics, National Institute for Materials Science, 1-1 Namiki, Tsukuba 305-0044, Japan

E-mail: ghkim@skku.edu

Received 19 November 2020, revised 26 January 2021
Accepted for publication 8 February 2021
Published 2 March 2021

Abstract

The integration of electrical contact into 2D heterostructure is an essential approach to high-quality electronic nano-devices, especially field-effect transistors. However, high contact resistance with transition metal dichalcogenides such as molybdenum disulphide (MoS_2)-based devices has been a significant fabrication impediment to their potential applications. Here, we have demonstrated the advantage of 1D indium metal contact with fully encapsulated MoS_2 within hexagonal boron nitride. The electrical measurements of the device exhibit ambipolar transport with an on/off ratio of 10^2 for holes and 10^7 for electrons. The device exhibits high field-effect mobility of 40.7 $cm^2\ V^{-1}\ s^{-1}$ at liquid nitrogen temperature. Furthermore, we have also analysed the charge-transport mechanism at the interface and have calculated the Schottky barrier height from the temperature-dependent measurement. These results are highly promising for the use of air-sensitive material heterostructure and large-scale design of trending flexible, transparent electronic wearable devices.

Supplementary material for this article is available online

Keywords: molybdenum sulphide, transition metal dichalcogenides, edge contact, contact resistance, Schottky barrier height

(Some figures may appear in colour only in the online journal)

1. Introduction

Transition metal dichalcogenides (TMDs) have the potential to replace conventional Si electronics because of their ultra-thinness, which allows for effective low-voltage electrostatic gating [1]. Along with atomic-scale thickness, these materials also demonstrate remarkable electrical and optical properties [2–4]. Among the TMDs, molybdenum disulphide (MoS_2) appears to be one of the most promising candidates in the 2D family due to its sizeable band gap, high on/off ratio and the possibility for large-scale synthesis through chemical vapour deposition [5–7]. Moreover, the ultra-flat surface without dangling bonds of MoS_2 presents the ability of weak van der Waals bonding with other 2D materials, leading to further utilisation of MoS_2 for novel electronic or optoelectronic applications via stacking [8]. With regard to future applications, MoS_2 is able to be used as field-effect transistors (FETs) [9–11], light-emission diodes [12], solar cells [13] and photodetectors [14, 15].

High contact resistance is one of the major obstacles in realising high-performance electronic devices based on MoS_2 and other TMD materials. The presence of the Schottky

barrier at the metal and MoS_2 interface results in increased contact resistance and, therefore, substantially degrades the electrical performance of the MoS_2-based devices [16]. In principle, as the Schottky–Mott rule [17–19] illustrated, the Schottky barrier height (SBH) depends upon the difference between the conduction-band edge or valence-band edge for *n*-type or *p*-type transistors and the contact metal work function, respectively [20]. However, the researcher found that in actual MoS_2 devices, the SBH deviates from the predicted value of the Schottky–Mott rule [19, 21, 22]. This deviation from the expected value was explained by the Bardeen theory [23], which takes into consideration the presence of traps, interface states and other imperfections at the contact metal-TMD interface [24]. This concept is termed Fermi-level pinning (FLP), and the extent of FLP is quantified by the pinning factor S, such that $S = 1$ indicates no pinning and $S = 0$ as complete pinning [22, 25]. Several solutions were proposed to address the issue of SBH and FLP. These solutions include the introduction of a thin dielectric layer between the metals and TMDs [26], semi-metal as a contact material for MoS_2, degenerate doping of the contact region and phase-engineered contacts [21]. Recently, a study suggested the transferring of pre-patterned electrodes on TMDs instead of direct deposition by evaporation [27, 28]. However, despite all these studies, the performance of TMD-based devices is still inferior to conventional silicon devices. Furthermore, these methods show limitations in the reproducibility and stability of the devices. It is theoretically predicted that 1D edge contact to MoS_2 would provide strong orbital overlap between the metal and MoS_2 and, therefore, result in thinner tunnel barriers and low resistance compared to top contacts [29].

In this work, we present the metal edge contact with MoS_2 because of its high performance, convenience and reliability. The indium edge contacts were realised by developing a plasma etching method followed by a rapid thermal annealing process. Indium was chosen as the contact metal because of its suitable work function. The metal with appropriate work function can reduce the Schottky barrier and contact resistance to some degree [16]. In this device, we have been able to achieve ambipolar transport in MoS_2 with an on/off ratio of 10^7 for electrons and 10^2 for holes. The transport behaviour was further analysed by calculating the SBH through temperature-dependent electrical measurement. We also calculated the contact resistance of the device, which shows the domination of edge contact over other contact methods.

2. Results and discussion

Figures 1(a) and (b) illustrate the sample design of MoS_2 1D edge contact (M1C) FETs. In preparation, standard 1 cm^2 heavily doped *p*-type Si/SiO_2 (oxide thickness of 285 nm) substrates were cleaned thoroughly in acetone and isopropyl alcohol in an ultrasonic sonicator for 10 min each, respectively. A six-layer MoS_2 flake was mechanically exfoliated from commercial bulk MoS_2 on a substrate using the Scotch tape method and identified by an optical microscope [30]. The Raman spectra of the six-layer MoS_2 are shown in figure 1(c), which confirms the flake we have used in this experiment was indeed MoS_2. We obtained two main vibrational modes, the E_{2g} peak located at $\sim$382 cm^{-1} represents the in-plane vibrational mode of both metal and chalcogen atoms, while the A_{1g} peak at $\sim$407 cm^{-1} represents the out-of-plane vibrational mode of only chalcogen atoms [31, 32]. Similarly, hBN flakes (5 $\sim$ 30 nm) were obtained by utilising the same procedure. All the exfoliated flakes were immediately moved to an Argon glove box. The dry transfer method by Poly (bisphenol A carbonate) described in previous research was employed for making our $hBN/MoS_2/hBN$ heterostructure [33]. Poly (methyl methacrylate) (PMMA) was spin coated and consolidated on a 160 °C hot plate for 2 min. Markers and electrodes were patterned by standard electron beam lithography. The etching process was performed in a reactive ion etching mini-plasma machine using a mixture of CF_4 and O_2 (1: 10 sccm). The In/Au (15/40 nm) contacts were deposited by e-beam evaporator (Korea Vacuum Tech. KVT-2004) followed by lift-off in acetone. After the first measurement, the samples were annealed through 1000 sccm Argon gas at 150 °C for 2 h in a rapid thermal annealing (Nextron RTP-1200) system and measured again. In our study, two-terminal and four-terminal measurement in a high-vacuum probe station with the pressure below 20 mTorr was performed to study the electrical properties of the M1C device.

Figure 2(a) presents the transfer characteristics of the M1C device in a range of −60 to 60 V before and after annealing. From the transfer characteristics, it is obvious that before annealing, the device exhibits *n*-type transport with a current on/off ratio of around 10^3 and a maximum on current of 63 nA at $V_G = 60$ V. After annealing, several changes can be observed. First, the device now exhibits ambipolar transport with a current on/off ratio of 10^7 for electrons (positive gate bias) and 10^2 for holes (negative gate bias). Second, the on current in the *n*-region (positive gate bias) has increased around 100 times from 63 nA to 6.8 μA. There was negligible current before annealing for the *p*-region (negative gate bias). However, after the annealing process, the maximum on current increased to approximately 10 nA. The inset figure exhibits the output characteristic of the device. The drastic change in the characteristic curves is attributed to argon annealing, which can improve the device performance by removing impurities, trapped bubbles, wrinkles and strain or chemical residue from the fabrication process, thus enhancing the bonding between the contact metal and MoS_2 [34]. Overall, the edge contact samples exhibited highly improved performance. For comparison, we also prepared several indium top contact devices with similar MoS_2 thickness under similar fabrication conditions. In all of these devices, the measured value of the contact resistance was almost ten times higher than the edge contact device. The transport characteristic measurements and calculation are shown in figure S1 (available online at stacks.iop.org/NANO/32/215701/mmedia).

MoS_2 typically demonstrates *n*-type transport and the observation of ambipolar transport in MoS_2 is quite rare. The

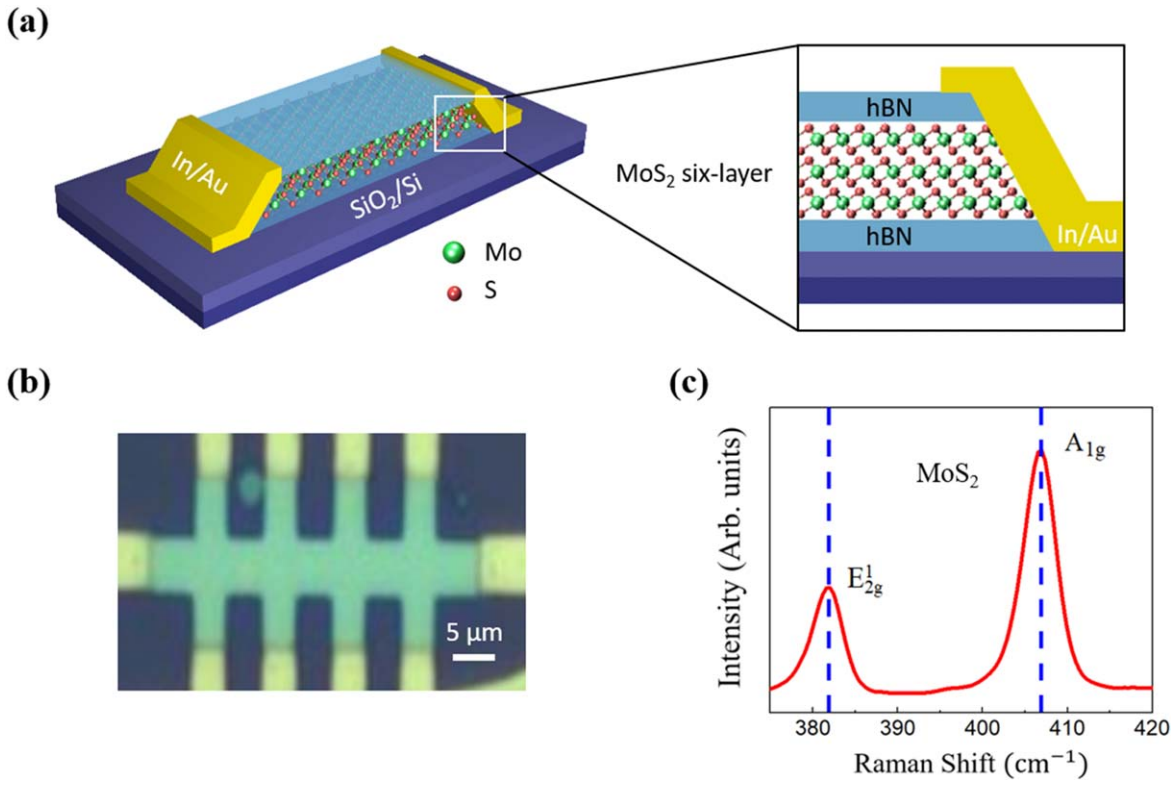

Figure 1. (a) Schematic illustrating the structure of the MoS_2 edge contact device with the expanded section showing the detail of the edge part. (b) Optical microscope image of the MoS_2-incapsulated device with In used for deposition. (c) Raman spectra of the device illustrating signature six-layer MoS_2 peaks.

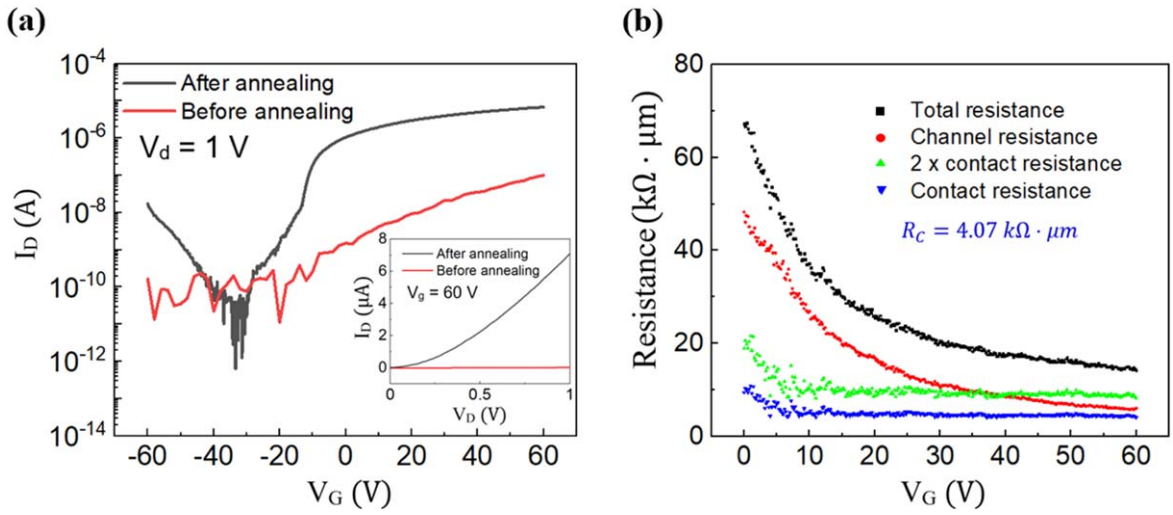

Figure 2. (a) Transfer curve of the M1C device at a drain voltage of 1 V, before and after the annealing process in semi-log scale (Inset shows the same device output curve before and after annealing). (b) Variation in total resistance, channel resistance and contact resistance of the M1C device as a function of gate voltage after the annealing process.

major reason behind this is the pinning of the Fermi level in MoS_2 [21, 22]. Studies have shown that the Fermi level in MoS_2 devices is pinned near the conduction band, thus not only resulting in Schottky barrier for electrons but making it extremely difficult to access the holes in the valence band [22]. However, the presence of ambipolar transport in this device indicates that either the Fermi-level pinning position has been changed in the MoS_2 band gap or it has been unpinned. Figure 2(b) presents the four-terminal measurement of the device to differentiate between the contact resistance and channel resistance. The equation $R_{total} = R_{channel} + 2R_{contact}$ has been used to calculate the contact resistance. At low gate voltages (0–20 V), the channel resistance is the dominant resistance that limits the current flow. However, as the gate voltage is increased, the channel resistance starts to reduce as the channel gets populated with gated-induced carriers (electrons). From $V_G = 37\ V$ onwards, the channel

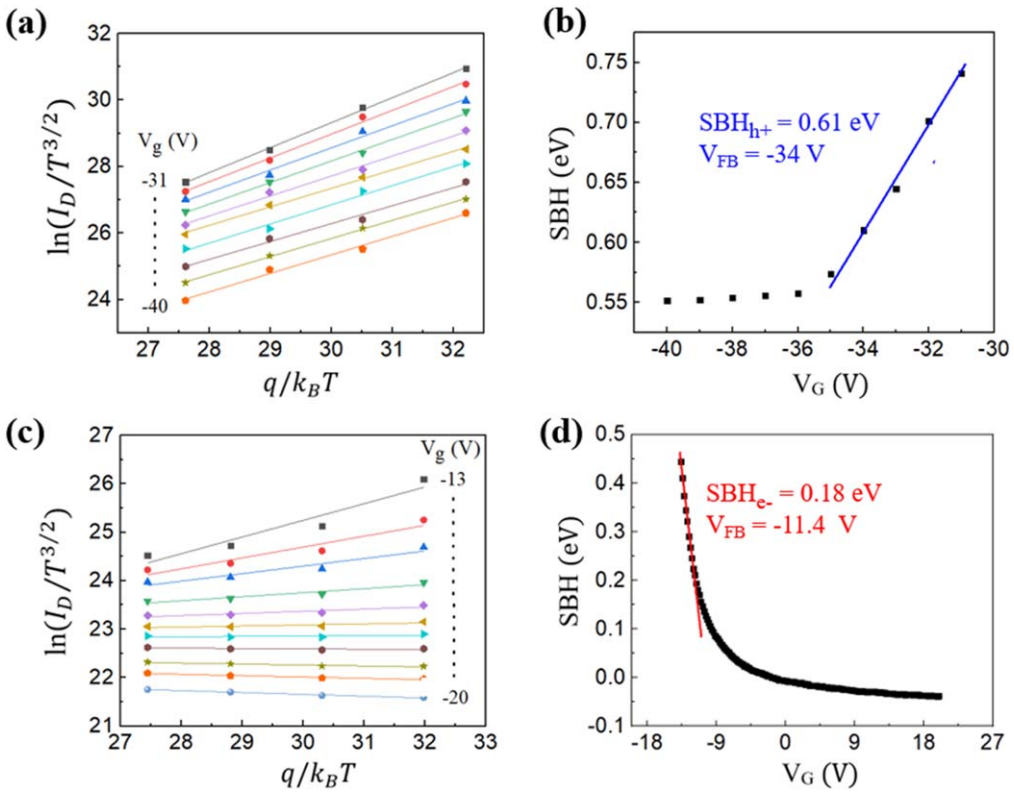

Figure 3. (a) and (c) are the SBH calculation in detail. $\ln(I_D/T^{3/2})$ was plotted against q/k_BT at different back-gate voltages for extracting the SBH for holes and electrons, respectively. (b) and (d) exhibit the SBH of the 1D edge contact FET device for electrons and holes as a function of gate voltage.

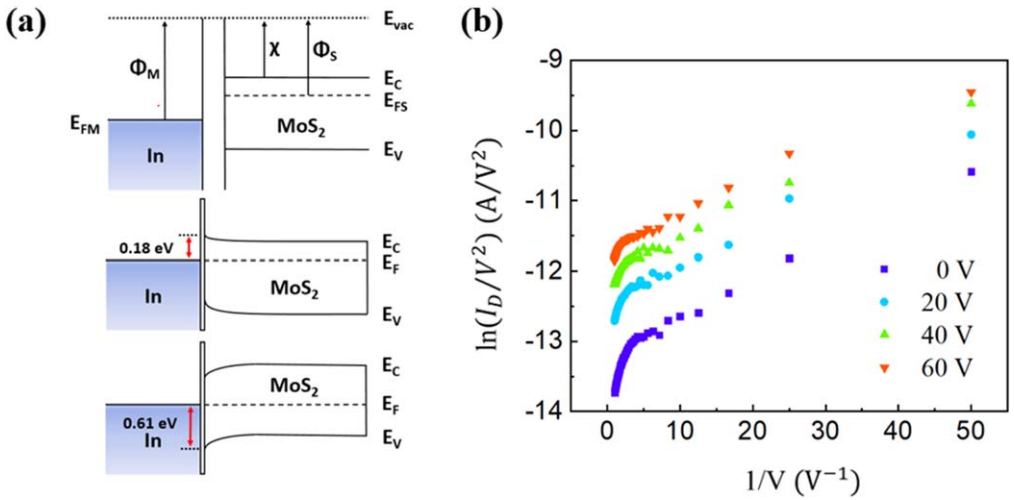

Figure 4. (a) Band diagrams showing the formation of SBH due to band bending at the interface of indium and MoS_2. (b) $\ln(I_D/V^2)$ are plotted as a function of the inverse of drain bias voltage $(1/V)$ indicating the tunnelling behaviour of the device at different gate voltages.

resistance becomes less than the contact resistance. The major current limiting resistance in this region is contact resistance with a value of 4.07 kΩμm at $V_G =$ 60 V. In comparison with the surface contact device shown in the supporting information, the contact resistance for the edge contact device is much lower.

From the transfer characteristic, we also calculated the field-effect mobility based on equation (1) [35], where $V_D = 1$ V, $L = 15.2 \times 10^{-4}$ cm and $W = 3.8 \times 10^{-4}$ cm are the length and width of the channel, respectively. $C_i = 1.21 \times 10^{-8}$ Fcm^{-2} is the gate insulator capacitance per unit area. The obtained value of mobility is 32 cm^2 V^{-1} s^{-1} at room temperature and a significantly higher value of 40.7 cm^2 V^{-1} s^{-1} at 77 K. The calculated value of the field-effect mobility is higher at low temperature as the phonon scattering reduces at low temperatures.

$$\mu = k \times \frac{L}{W} \times \frac{1}{V_D} \times \frac{1}{C_i}. \quad (1)$$

In order to quantitatively evaluate the SBH in the device, we performed electrical characterisation at different temperatures (77–420 K), as shown in figure S2. Figure S2 displays the transfer curves of the device at various temperatures with the source–drain current in log scale. Equation (3) can be used to describe the carrier transport at Schottky contacts [36].

$$I_D = WA^*_{2D}T^{3/2}\exp\left(-\frac{q\varnothing_{Bn}}{k_BT}\right)\exp\left(\frac{qV_D}{k_BT}\right), \tag{2}$$

$$A^*_{2D} = \frac{q\sqrt{8\pi m^* {k_B}^3}}{h^2}$$

$$\varnothing_{Bn} = \frac{k_B}{q}\left[-\frac{\Delta \ln\left(I_D/T^{3/2}\right)}{\Delta T^{-1}}\right]. \tag{3}$$

In equations (2) and (3), W is the channel width, q is the electron charge, k_B is the Boltzmann constant, A^*_{2D} is the Richardson constant, $\varnothing_{Bn}$ is the SBH, V_D is the drain voltage and m^* is the effective mass. Equation (3), derived from equation (2), is used to extract the SBH from the slope of the linear fit to $\ln\left(I_D/T^{3/2}\right)$ as a function of q/k_BT. In these measurements, a constant drain voltage of 1 V was applied. The application of such a high drain voltage could reduce the influence of the Schottky barrier at the drain and the current will be effectively determined by the Schottky barrier at the source [21].

To obtain the value of the SBH, first we calculated $\ln\left(I_D/T^{3/2}\right)$ and plotted it as a function of q/k_BT at various gating biases, as shown in figures 3(a) and (c). Then, we extracted the slope from all these plots using the linear fitting, which resulted in negative SBH. These negative slopes were plotted as a function of gate voltage as the true SBH. The SBH for the electron and hole transport are 0.18 eV at flat-band voltage $V_{FB} = -11.4$ V and 0.61 eV at $V_{FB} = -34$ V, respectively, as shown in figures 3(b) and (d).

As can be seen in figure 4(a), the contacts in our device are Schottky and it is well known that in the presence of Schottky barrier at the interface, tunnelling through the barrier is the dominant mechanism for charge transfer across the barrier [37]. The tunnelling behaviour could be a direct tunnel or Fowler–Nordheim (FN) tunnel depending on the shape and width of the barrier. To gain further insight into the transport across the barrier in our device, direct (4*a*) and the FN tunnelling (5*a*) equations were used, and to graphically see the linearity of the data and for easy comparison, equations (4*b*) and (5*b*) are extracted from equations (4*a*) and (5*a*), respectively. [38, 39].

Direct tunnelling:

$$I_D \propto V\exp\left[-\frac{4\pi d\sqrt{2m^*\varnothing_B}}{h}\right], \tag{4a}$$

$$\ln\left(\frac{I_D}{V^2}\right) \propto \ln\left(\frac{1}{V}\right) - \left[\frac{4\pi d\sqrt{2m^*\varnothing_B}}{h}\right]. \tag{4b}$$

FN tunnelling:

$$I_D \propto V^2\exp\left[-\frac{8\pi d\sqrt{2m^*\varnothing_B^3}}{3hqV}\right], \tag{5a}$$

$$\ln\left(\frac{I_D}{V^2}\right) \propto -\frac{1}{V}\left[\frac{8\pi d\sqrt{2m^*\varnothing_B^3}}{3hq}\right]. \tag{5b}$$

Here, $\varnothing_B$ is the barrier height, m is the free electron mass, $m^*(0.46\ m)$ [40] is the effective mass of electrons in the MoS_2 channel, q is the electron charge, h is Planck's constant and d is the width of the barrier. Figure 4(b) provides a plot between $\ln\left(I_D/V^2\right)$ and $1/V$ at different gate voltages. The graph remains linear for the range $1/V = 10$ to 50 V^{-1} and as evident from equation (4*b*), the linear region indicates direct tunnelling. So, for a drain voltage of 0.02–0.1 V, the device exhibits direct tunnelling. Whereas, the graph in figure 4(b) exhibits exponential behaviour for a range $1/V = 1$to 10 V^{-1}. This proves that for a drain voltage of 0.1–1 V, the device shows FN tunnelling. This change in tunnelling behaviour has been attributed to change in the shape of a barrier as the drain voltage is increased and these findings are consistent with the previous reports on transport across the Schottky barrier [37].

3. Conclusion

We have demonstrated the use of indium as a successful metal for the encapsulated MoS_2 1D edge contact gate tuneable device. The van der Waals heterostructure with a high-vacuum rapid thermal annealing process dramatically reduces the interfacial impurities. It provides a standard platform that allows us to achieve a high-mobility 2D device through a range of temperature-dependent electrical transport measurements. The systematic four-terminal studies have revealed better contact resistance compared to other types of contacts. Furthermore, detailed calculated SBH results have indicated that direct tunnelling behaviour is the theoretical match for the observed charge-transfer mechanism. Our work shows the premeditated design and contact method as a simple avenue to improve charge-transportation performance for investigating TMD 2D materials and potential applications in future flexible and transparent devices.

Acknowledgments

This work was supported by the National Research Foundation of Korea (NRF) funded by the Korea government (MSIT) (Grant Nos. 2019R1A2C2088719 and 2018R1D1A1B07048985). K W and T T acknowledge support from the Elemental Strategy Initiative conducted by the MEXT, Japan (Grant No. JPMXP0112101001), JSPS KAKENHI (Grant No. JP20H00354) and the CREST (Grant No. JPMJCR15F3), JST.

Data availability statement

The data generated and/or analysed during the current study are not publicly available for legal/ethical reasons but are available from the corresponding author on reasonable request.

ORCID iDs

Kenji Watanabe https://orcid.org/0000-0003-3701-8119
Gil-Ho Kim https://orcid.org/0000-0002-5153-4235

References

[1] Manzeli S, Ovchinnikov D, Pasquier D, Yazyev O V and Kis A 2017 2D transition metal dichalcogenides *Nat. Rev. Mater.* **2** 17033
[2] Allain A, Kang J, Banerjee K and Kis A 2015 Electrical contacts to two-dimensional semiconductors *Nat. Mater.* **14** 1195–205
[3] Newaz A K M, Prasai D, Ziegler J I, Caudel D, Robinson S, Haglund R F and Bolotin K I 2013 Electrical control of optical properties of monolayer MoS_2 *Solid State Commun.* **155** 49–52
[4] Lopez-Sanchez O, Lembke D, Kayci M, Radenovic A and Kis A 2013 Ultrasensitive photodetectors based on monolayer MoS_2 *Nat. Nanotechnol.* **8** 497–501
[5] Kumar N, Tomar R, Wadehra N, Devi M M, Prakash B and Chakraverty S 2018 Growth of highly crystalline and large scale monolayer MoS_2 by CVD: the role of substrate position *Cryst. Res. Technol.* **53** 1–7
[6] Zhou D, Shu H, Hu C, Jiang L, Liang P and Chen X 2018 Unveiling the growth mechanism of MoS_2 with chemical vapor deposition: from two-dimensional planar nucleation to self-seeding nucleation *Cryst. Growth Des.* **18** 1012–9
[7] Jeon J, Jang S K, Jeon S M, Yoo G, Jang Y H, Park J H and Lee S 2015 Layer-controlled CVD growth of large-area two-dimensional MoS_2 films *Nanoscale* **7** 1688–95
[8] Khan M A *et al* 2018 High performance self-gating graphene/MoS_2 diode enabled by asymmetric contacts *Nanotechnology* **29** 1–5
[9] Khan M A, Rathi S, Lim D, Yun S J, Youn D H, Watanabe K, Taniguchi T and Kim G H 2018 Gate tunable self-biased diode based on few layered MoS_2 and WSe_2 *Chem. Mater.* **30** 1011–6
[10] Andleeb S, Eom J, Rauf Naz N and Singh A K 2017 MoS_2 field-effect transistor with graphene contacts *J. Mater. Chem.* C **5** 8308–14
[11] Tong X, Ashalley E, Lin F, Li H and Wang Z M 2015 Advances in MoS_2-based field effect transistors (FETs) *Nano-Micro Lett.* **7** 203–18
[12] Lu G Z *et al* 2019 Electrically pumped white-light-emitting diodes based on histidine-doped MoS_2 quantum dots *Small* **15** 1–8
[13] Tsai M L, Su S H, Chang J K, Tsai D S, Chen C H, Wu C I, Li L J, Chen L J and He J H 2014 Monolayer MoS_2 heterojunction solar cells *ACS Nano* **8** 8317–22
[14] Venkatesan A, Rathi S, Kim Y, Kim H, Whang D, Yun S J and Kim G H 2020 Few-layer $PdSe_2$-based field-effect transistor for photodetector applications *Mater. Sci. Semicond. Process.* **115** 105102
[15] Huang Z, Han W, Tang H, Ren L, Chander D S, Qi X and Zhang H 2015 Photoelectrochemical-type sunlight photodetector based on MoS_2/graphene heterostructure *2D Mater.* **2** 035011
[16] Kang J, Sarkar D, Liu W, Jena D and Banerjee K 2012 A computational study of metal-contacts to beyond-graphene 2D semiconductor materials *Tech. Dig. - Int. Electron Devices Meet. IEDM* 407–10
[17] Mott N F 1939 The theory of crystal rectifiers *Proc. R. Soc. Lond.* **171** 27–38
[18] Schottky W 1938 Halbleitertheorie der sperrschicht *Naturwissenschaften* **26** 843
[19] Tung R T 2014 The physics and chemistry of the Schottky barrier height *Appl. Phys. Rev.* **1** 011304
[20] Thanailakis A and Northrop D C 1973 Metal-germanium Schottky barriers *Solid State Electron.* **16** 1383–9
[21] Kim C, moon I, Lee D, Choi M S, Ahmed F, Nam S, Cho Y, Shin H J, Park S and Yoo W J 2017 Fermi level pinning at electrical metal contacts of monolayer molybdenum dichalcogenides *ACS Nano.* **11** 1588–96
[22] Yang Z *et al* 2019 A Fermi-level-pinning-free 1D electrical contact at the intrinsic 2D MoS_2–metal junction *Adv. Mater.* **31** 1–9
[23] Bardeen J 1947 Surface states and rectification at a metal semi-conductor contact *Phys. Rev.* **71** 717–27
[24] Hu Z, Wu Z, Han C, He J, Ni Z and Chen W 2018 Two-dimensional transition metal dichalcogenides: interface and defect engineering *Chem. Soc. Rev.* **47** 3100–28
[25] Sotthewes K, Van Bremen R, Dollekamp E, Boulogne T, Nowakowski K, Kas D, Zandvliet H J W and Bampoulis P 2019 Universal Fermi-level pinning in transition-metal dichalcogenides *J. Phys. Chem.* C **123** 5411–20
[26] Schmidt H, Giustiniano F and Eda G 2015 Electronic transport properties of transition metal dichalcogenide field-effect devices: surface and interface effects *Chem. Soc. Rev.* **44** 7715–36
[27] English C D, Shine G, Dorgan V E, Saraswat K C and Pop E 2016 Improved contacts to MoS_2 transistors by ultra-high vacuum metal deposition *Nano Lett.* **16** 3824–30
[28] Smithe K K H, English C D, Suryavanshi S V and Pop E 2017 Intrinsic electrical transport and performance projections of synthetic monolayer MoS_2 devices *2D Mater.* **4** 011009
[29] Celani A, Villermaux E and Vergassola M 2014 Odor landscapes in turbulent environments *Phys. Rev.* X **4** 1–17
[30] Novoselov K S, Geim A K, Morozov S V and Jiang D 2004 PGR Tips on writing effective CVs *Phys. Rev. Lett.* **306** 666–9
[31] Wang X, Li Y, Zhuo L, Zheng J, Peng X, Jiao Z, Xiong X, Han J and Xiao W 2018 Controllable growth of two-dimensional WSe_2 using salt as co-solvent *CrystEngComm.* **20** 6267–72
[32] Jiang H 2012 Electronic band structures of molybdenum and tungsten dichalcogenides by the GW approach *J. Phys. Chem.* C **116** 7664–71
[33] Purdie D G, Pugno N M, Taniguchi T, Watanabe K, Ferrari A C and Lombardo A 2018 Cleaning interfaces in layered materials heterostructures *Nat. Commun.* **9** 1–12
[34] Jain A, Bharadwaj P, Heeg S, Parzefall M, Taniguchi T, Watanabe K and Novotny L 2018 Minimizing residues and strain in 2D materials transferred from PDMS *Nanotechnology* **29** 265203
[35] Zhan Y, Liu Z, Najmaei S, Ajayan P M and Lou J 2012 Large-area vapor-phase growth and characterization of MoS_2 atomic layers on a SiO_2 substrate *Small* **8** 966–71
[36] Anwar A, Nabet B, Culp J and Castro F 1999 Effects of electron confinement on thermionic emission current in a modulation doped heterostructure *J. Appl. Phys.* **85** 2663–6
[37] Ahmed F, Choi M S, Liu X and Yoo W J 2015 Carrier transport at the metal-MoS_2 interface *Nanoscale.* **7** 9222–8
[38] Beebe J M, Kim B, Gadzuk J W, Frisbie C D and Kushmerick J G 2006 Transition from direct tunneling to field emission in metal-molecule-metal junctions *Phys. Rev. Lett.* **97** 1–4
[39] Sarker B K and Khondaker S I 2012 Thermionic emission and tunneling at carbon nanotube-organic semiconductor interface *ACS Nano.* **6** 4993–9
[40] Das S, Prakash A, Salazar R and Appenzeller J 2014 Toward low-power electronics: Tunneling phenomena in transition metal dichalcogenides *ACS Nano.* **8** 1681–9